Structural dynamics in hybrid halide perovskites: Bulk Rashba splitting, spin texture, and carrier localization

Chao Zheng,[1] Shidong Yu,[1,2] and Oleg Rubel[1,*]

[1]*Department of Materials Science and Engineering, McMaster University, 1280 Main Street West, Hamilton, Ontario L8S 4L8, Canada*
[2]*College of Materials Science and Engineering, Jilin University, 2699 Qianjin Street, Changchun City 130012, China*

The extended charge carrier lifetime in hybrid halide perovskites was attributed to a quasi-indirect band gap that arises due to a Rashba splitting in both conduction and valence band edges. In this paper, we present results for an effective relativistic band structure of $(CH_3NH_3)PbI_3$ with the focus on the dispersion of electronic states near the band edges of $(CH_3NH_3)PbI_3$ affected by thermal structural fluctuations. We establish a relationship between the magnitude of the Rashba splitting and a deviation of the Pb atom from its centrosymmetric site position in the PbI_6 octahedron. For the splitting energy to reach the thermal energy $k_BT \approx 26$ meV (room temperature), the displacement should be on the order of 0.3 Å, which is far above the static displacements of Pb atoms in the tetragonal phase of $(CH_3NH_3)PbI_3$. The significant dynamic enhancement of the Rashba splitting observed at earlier simulation times (less than 2 ps) later weakens and becomes less than the thermal energy despite the average displacement of Pb atoms remaining large (0.37 Å). A randomization of Pb-displacement vectors and associated cancellation of the net effective magnetic field acting on electrons at the conduction band edge is responsible for reduction of the Rashba splitting. The lattice dynamics also leads to deterioration of a Bloch character for states in the valence band leading to the subsequent localization of holes, which affects the bipolar mobility of charge carriers in $(CH_3NH_3)PbI_3$. These results call into question the quasi-indirect band gap as a reason for the long carrier lifetime observed in $(CH_3NH_3)PbI_3$ at room temperature. Analysis of spin projections and the spin overlap at the band edges also rules out the spin helicity as a possible cause for a long lifetime of optical excitations in perovskite structures. An alternative mechanism involves dynamic localization of holes and their reduced overlap with electrons in reciprocal space.

I. INTRODUCTION

Hybrid halide perovskites, with $(CH_3NH_3)PbI_3$ being a prominent member, have attracted enormous interest as a solar cell absorber material [1–5]. One unique property of this class of materials is that they combine benefits of direct and indirect semiconductors featuring both a long carrier lifetime in excess of 100 ns [6–9] and a sharp absorption edge [10]. These features are attributed to the presence of Rashba splitting, which occurs at the valence and conduction band edges of hybrid halide perovskites [11–13].

The physics of the Dresselhaus-Rashba effect [14,15] is linked to the spin-orbit coupling (SOC) due to an interaction between electron spin and an apparent magnetic field that arises from the electron moving in an electric field. Not all electronic states are directly susceptible to SOC. The coupling affects states that experience a net apparent magnetic field remaining after averaging over possible electron trajectories. In atoms, this leads to splitting of energy levels for states with the orbital angular momentum quantum number $\ell > 0$. In solids, electron orbitals experience an additional crystal field. If the crystal field lacks a central symmetry, Kramers' spin degeneracy is lifted leading to spin splitting and occurrence of an unusual band dispersion illustrated in Fig. 1(a). The

Dresselhaus-Rashba effect is actively studied in spintronics (spin currents and the spin Hall effect) and topological insulators [16].

The extended carrier lifetime in hybrid halide perovskites was attributed to a quasi-indirect band gap that arises due to Rashba splitting in both conduction and valence band edges [17–19] as shown in Fig. 1(b). For this argument to stand, the magnitude of Rashba splitting must significantly exceed the solar cell operating temperature ($E_R > k_BT$) to prevent the finite-temperature population statistics from enabling direct optical transitions [Fig. 1(b)]. Niesner *et al.* [20] measured the valence band dispersion in $(CH_3NH_3)PbI_3$ using an angle-resolved photoelectron spectroscopy and found a rather large magnitude of Rashba splitting of $E_R = 0.16$ and 0.24 eV in orthorhombic (low temperature) and cubic (high temperature) phases, respectively, indicating that the splitting is enhanced by the lattice dynamics. Recent photogalvanic measurements [21] provide more moderate values of the combined (valence and conduction band) Rashba splitting of $E_R \sim 0.1$ eV that steadily increases with temperature.

Typically, the band structure of perovskites is calculated using a primitive unit cell (either pseudocubic, tetragonal, or orthorhombic structures), where atoms are relaxed to their lowest energy positions [22,23]. However, experimental studies of hybrid halide perovskites [24,25] clearly indicate a substantial dynamic disorder of atomic positions at room
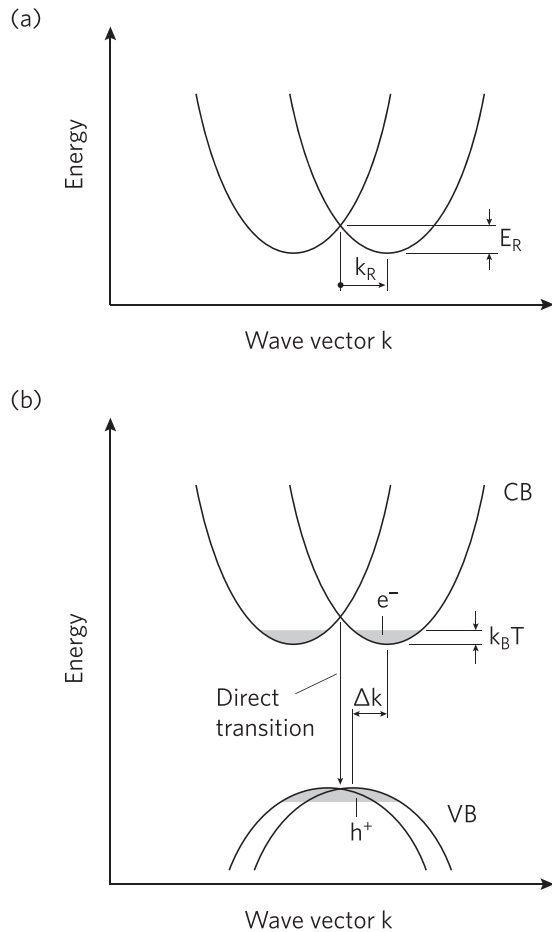
————
[*]rubelo@mcmaster.ca

(a)

(b)

FIG. 1. (a) Schematic Dresselhaus-Rashba splitting with E_R showing the magnitude of splitting. (b) Although the band gap is indirect (Δk), the final temperature carrier statistic allows for direct transitions if $E_R < k_B T$.

temperature, which should influence the electronic structure of these materials. For the aforementioned mechanism to operate, the lattice dynamics should produce a steady enhancement of the Rashba splitting and, *at the same time*, preserve the Bloch character (wave vector k) for electronic states at the band edges. Theoretical studies of dynamic effects on the Rashba splitting started only recently [26–30], and details on how the dispersion of electronic states near the band edges of $(CH_3NH_3)PbI_3$ is affected by thermal structural fluctuations are still missing.

In this paper, we calculate an effective relativistic band structure of $(CH_3NH_3)PbI_3$ taking the thermal disorder of atomic positions into account. The disorder is explicitly modeled via *ab initio* molecular dynamics (MD) simulation performed for a large supercell. The supercell band structure is later unfolded to a primitive (pseudocubic) Brillouin zone that allows its direct comparison with experimental data. In addition, we explore a possible spatial localization of electronic states at the band edges caused by dynamical structural fluctuations. Robustness of electronic states at the band edges is an important functional requirement for photovoltaic applications.

II. COMPUTATIONAL DETAILS

The Vienna *Ab initio* Simulation Package (VASP) [31,32] density functional theory [33] (DFT) package was employed in this work. A Perdew, Burke, and Ernzerhof [34] (PBE) gradient approximation for the exchange-correlation functional was used in combination with the Grimme *et al.* [35] (D3) correction to capture long-range van der Waals interactions.

The original structure of tetragonal $(CH_3NH_3)PbI_3$ was taken from Stoumpos *et al.* [36] (database code ICSD 250739) with the following structural parameters: space group 108 (*I4cm*), $a = b = 8.849$ Å, $c = 12.642$ Å, fractional coordinates $u_{Pb} = (0, 0, 0)$, $u_{I1} = (0, 0, 0.24720)$, $u_{I2} = (0.21417, 0.71417, 0.00460)$. Once the PbI_3 cage was set, methylammonium cations were added, and the structure was relaxed while maintaining symmetry of the PbI_3 cage. Calculations were carried out using a $3 \times 3 \times 2$ Monkhorst and Pack [37] k mesh for the primitive Brillouin zone of a tetragonal phase. The structural relaxation was performed by minimizing Hellmann-Feynman forces and stresses below 20 meV/Å and 0.5 kbar, respectively. The cutoff energy for the plane-wave expansion was set at 400 eV. Relativistic effects (SOC) were omitted from the structure optimization but included later in band structure calculations. The resultant optimized structure had lattice parameters of $a = b = 8.661$ Å and $c = 12.766$ Å and can be accessed at the Cambridge Crystallographic Data Center (CCDC) under deposition No. 1870783.

Next we describe a semiempirical scaling of the lattice parameters to achieve a finite-temperature structure of $(CH_3NH_3)PbI_3$ that is self-consistent with the PBE+D3 functional. The volume of the calculated tetragonal unit cell at 0 K yields a pseudocubic lattice parameter of $a_c(0 \text{ K}) = 6.209$ Å. Changes in the pseudocubic lattice parameter with temperature can be expressed as

$$a_c(T) = a_c(0 \text{ K})(1 + \alpha_a T) \qquad (1)$$

with the linear expansion coefficient of $\alpha_a = 4.21 \times 10^{-5}$ K^{-1} inferred from the experimental data [24] in the range of temperatures 150–350 K [see Fig. 6(c) therein]. Evolution of the pseudocubic lattice parameter with temperature is shown in Fig. 2(a).

Tetragonality of the structure can be expressed as

$$t = 1 - a_t/c_t, \qquad (2)$$

where $a_t = b_t$ and c_t are tetragonally distorted lattice parameters that are related to conventional lattice parameters of the tetragonal structure via $a = a_t\sqrt{2}$ and $c = 2c_t$. At 0 K the tetragonality is $t(0 \text{ K}) = 0.04058$ as obtained from our DFT calculations. The tetragonality is significantly reduced with increasing temperature and amounts to $t(293 \text{ K}) = 0.01$ [36]. The temperature-dependent tetragonality can be captured by a scaling function [24]

$$t(T) = t(0)(1 - T/T_c)^{2\beta} \qquad (3)$$

with critical parameters $T_c = 333$ K and $\beta = 0.27$ taken from [24] [see Fig. 8(b) therein]. The temperature-dependent tetragonality parameter is shown in Fig. 2(b). The temperature-dependent tetragonally distorted lattice parameters $a_t(T)$ and $c_t(T)$ [Fig. 2(a)] were obtained by combining
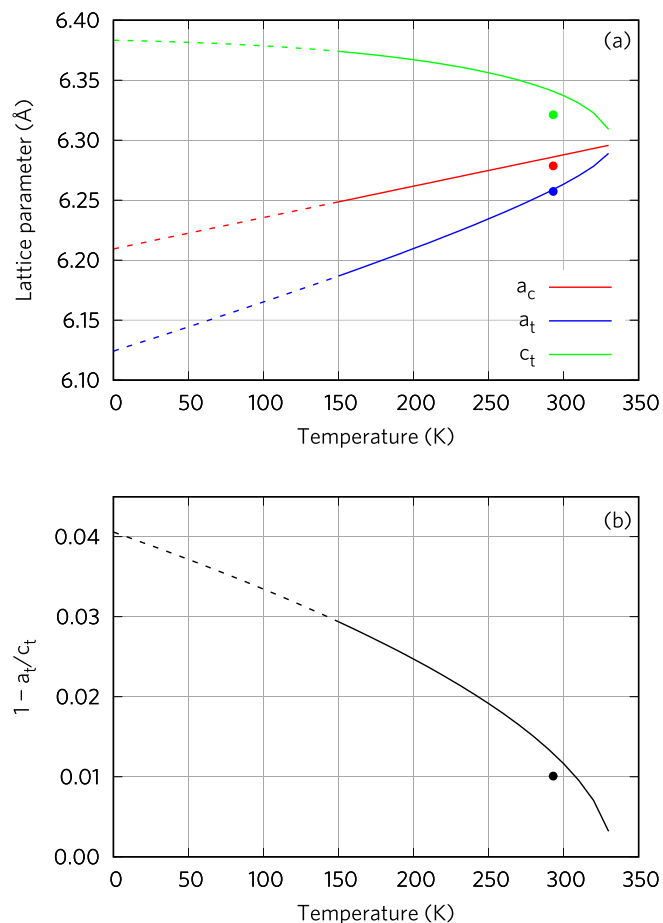
FIG. 2. Finite-temperature scaling of $(CH_3NH_3)PbI_3$ (a) lattice parameters and (b) tetragonality starting with DFT-PBE+D3 results for 0 K. Data are shown for $T < 150$ K even though the tetragonal structure is unstable in this temperature range. Experimental data [36] are shown with points.
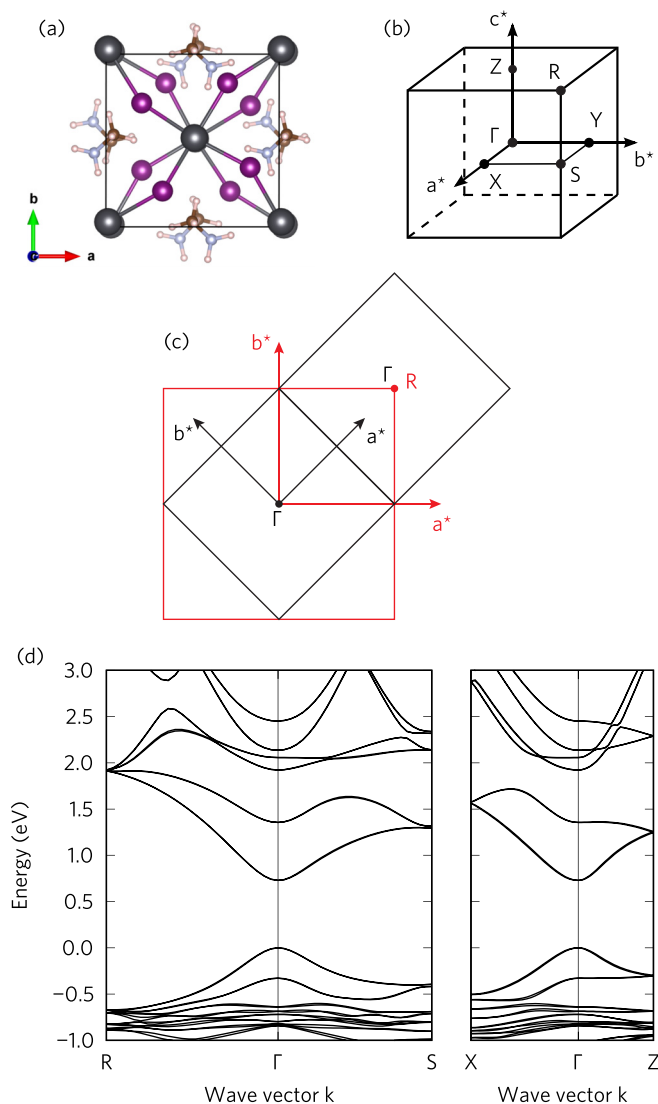

FIG. 3. (a) Tetragonal unit cell, (b) Brillouin zone, (c) folding of the R point into Γ when the structure is transformed from a pseudocubic (red) to a tetragonal (black) cell, and (d) relativistic band structure of tetragonal $(CH_3NH_3)PbI_3$ with lattice parameters scaled to 300 K and the symmetrized PbI_3 cage. No sizable Rashba splitting is observed although the structure is noncentrosymmetric. The origin of the energy scale is set at the Fermi energy.

the $t(T)$ and $a_c(T)$ dependencies assuming an equal volume for both cubic and tetragonal structures ($a_c^3 = c_t a_t^2$) at a given temperature.

This approach yields finite-temperature tetragonal lattice parameters of $a = b = 8.858$ Å and $c = 12.674$ Å at 300 K that are self-consistent with PBE+D3. Atomic positions of this structure were further relaxed while maintaining symmetry of the PbI_3 cage. The corresponding structure file can be accessed at CCDC under deposition No. 1870784.

The MD simulation was performed in two stages: first preheating and then a "production" run. The initial structure was a $4 \times 4 \times 4$ supercell [Fig. 9(a)] with lattice parameters scaled to 300 K as described above. The symmetry (except for the translational one) was turned off during the simulation (VASP tag ISYM = 0). Preheating from 0 to 300 K was performed in 500 steps (step size of 1 fs) using a linear ramp-up function (VASP tag SMASS = −1). Velocities were scaled every 10 MD steps. Accuracy of computed Hellmann-Feynman forces was determined by the energy convergence criterion of 10^{-7} eV. Only one k point at Γ was used to sample the Brillouin zone. Atomic positions and velocities at the end

of the preheating stage were taken as input for the production run. The production run took 2200 steps (step size of 1 fs) of a constant energy MD (VASP tag SMASS = −3). Atomic positions during MD were stored every 10 steps.

Band structure calculations were performed taking SOC into account. Although the band gap is underestimated at the DFT-PBE level of theory, the band dispersion and the Rashba splitting should be properly captured. The band structure of supercells was unfolded to a primitive Brillouin zone corresponding to a pseudocubic structure. The unfolding was performed with a "fold2Bloch" utility [38].

A spin texture was analyzed in the following way. The spinor wave function is represented as a linear combination
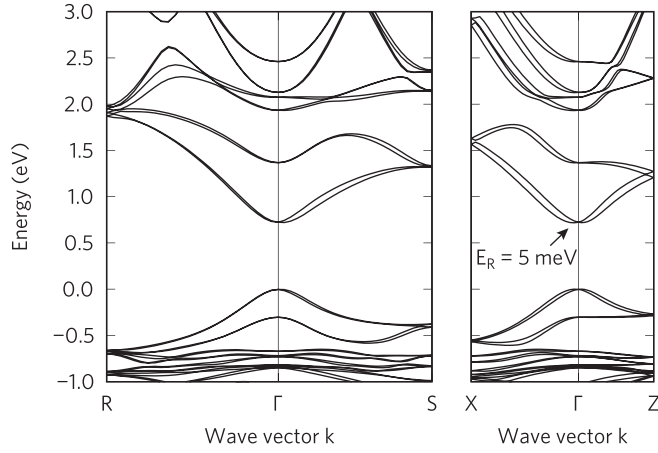
FIG. 4. Relativistic band structure of tetragonal $(CH_3NH_3)PbI_3$ with lattice parameters scaled to 300 K and relaxed PbI_3 cage. The Rashba splitting is present, but its magnitude is less that k_BT at room temperature.

of spin up and down components,

$$|\psi\rangle = \alpha|\uparrow\rangle + \beta|\downarrow\rangle = \begin{pmatrix} \alpha \\ \beta \end{pmatrix}, \qquad (4)$$
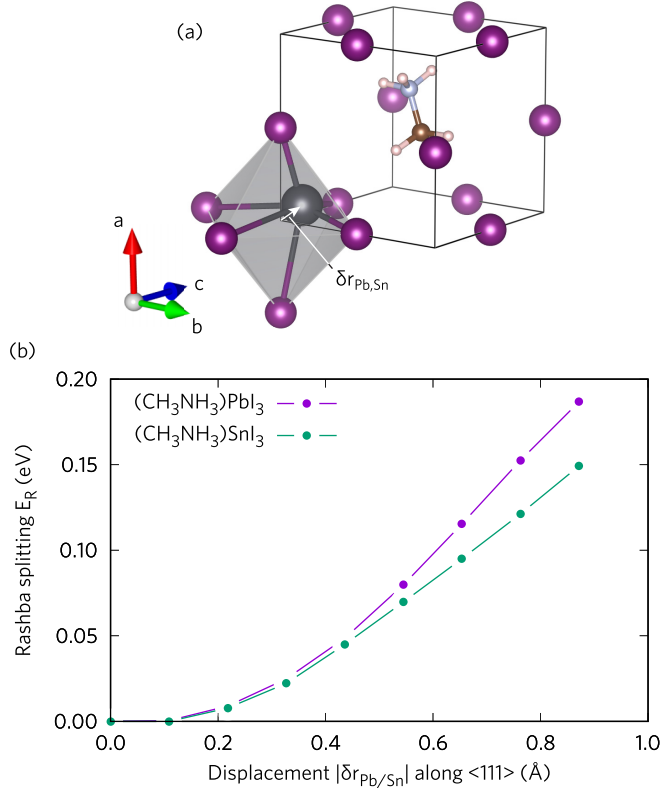

FIG. 5. (a) Displacement vector $\delta\boldsymbol{r}$ of the Pb or Sn atom from the center of the octahedron formed by iodine atoms. (b) Rashba splitting in a cubic structure as a function of the displacement of the Pb or Sn atom from its centrosymmetric position.
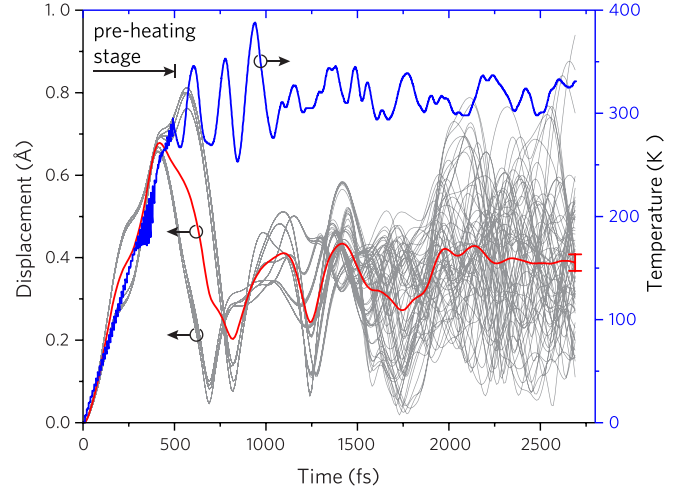

FIG. 6. Time evolution of a displacement δr_{Pb_i} of Pb atoms from the center of their individual octahedra (gray curves, left axis), the average $\langle\delta r_{Pb}\rangle$ for all Pb atoms in the supercell (red curve, left axis), and temperature T of the MD ensemble (blue curve, right axis). First 500 fs correspond to the preheating stage. Displacements fully dephase after approximately 2000 fs and $\langle\delta r_{Pb}(t)\rangle$ stabilizes.

that fulfill the normalization requirement $\alpha^2 + \beta^2 = 1$. Spin projections for individual eigenstates

$$\langle S_m \rangle = \langle \psi | \sigma_m | \psi \rangle \quad (m = x, y, z) \qquad (5)$$

were computed along Cartesian coordinates (VASP tag LORBIT = 11, PROCAR file). Here σ_m are Pauli matrices. The spin projections are related to spinor components as

$$\langle S_x \rangle = \alpha^*\beta + \beta^*\alpha, \qquad (6a)$$

$$\langle S_y \rangle = i(\beta^*\alpha - \alpha^*\beta), \qquad (6b)$$

$$\langle S_z \rangle = \alpha^2 - \beta^2. \qquad (6c)$$

It is possible to determine α and β from Eqs. (6) with the uncertainty of a phase factor $e^{i\theta}$, which affects neither the relative contribution of spin up/down components nor the spin overlap between two states. The uncertainty was resolved by constraining $\mathrm{Im}(\alpha) = 0$ that is consistent with eigenvectors of Pauli matrices.

The inverse participation ratio (IPR) χ was used as a measure of localization. It was evaluated on the basis of probabilities $\rho_n(E_i)$ of finding an electron with an eigenenergy E_i within a muffin tin sphere centered at an atomic site n [39,40]:

$$\chi(E_i) = \frac{\sum_n \rho_n^2(E_i)}{\left[\sum_n \rho_n(E_i)\right]^2}. \qquad (7)$$

Here the summation index n runs over all atomic sites.

III. RESULTS AND DISCUSSION

A. Static structures

We begin with presenting the electronic structure of tetragonal $(CH_3NH_3)PbI_3$ with lattice parameters scaled to $T = 300$ K and the PbI_3 cage symmetry [Fig. 3(a)] obtained from x-ray diffraction studies [36]. The quasidirect band gap is
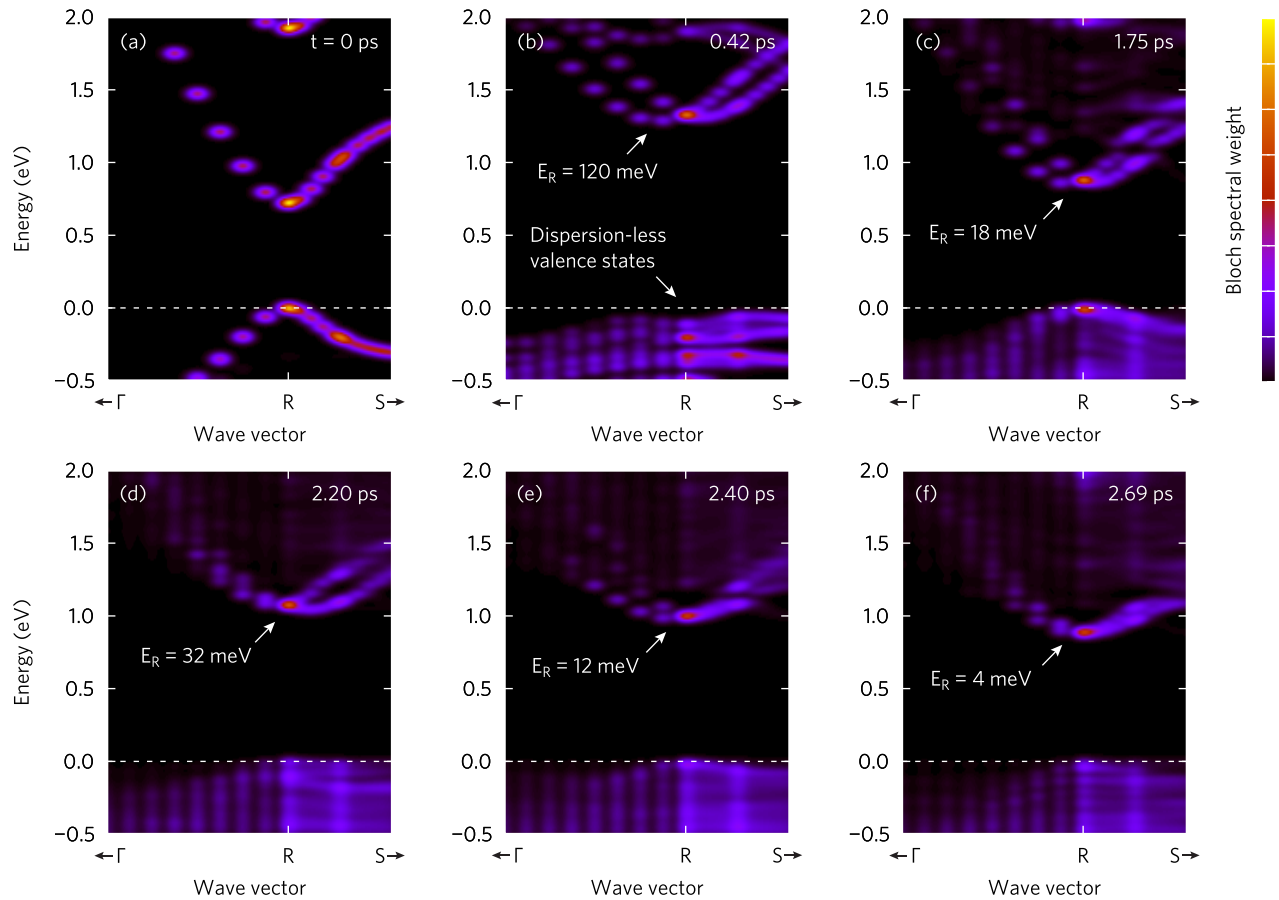
FIG. 7. Effective band structure of $4 \times 4 \times 4$ tetragonal $(CH_3NH_3)PbI_3$ supercell at different MD time snapshots: (a) $t = 0$, (b) 0.42 ps, (c) 1.75 ps, (d) 2.20 ps, (e) 2.40 ps, and (f) 2.69 ps. The Bloch character degrades at the VBE. Values for the Rashaba splitting E_R were derived from all eigenvalues in the calculation, including those that do not appear on the k path selected for the band structure plot. The strongest dynamical enhancement of E_R is observed at the initial time steps. Data points were smeared using a Gaussian function with the standard deviation of $\sigma_k = 0.0025 \, \text{Å}^{-1}$ in k space and $\sigma_E = 25$ meV on the energy scale.

typically observed at the R point of the Brillouin zone [Fig. 3(b)]. However, the R point is folded into Γ in the tetragonal phase [Fig. 3(c)]. The corresponding band structure is presented in Fig. 3(d) and shows no Rashba splitting as also noticed in Ref. [26]. A small nondegeneracy occurs at the band edges due to the field from methylammonium cations.

Experimentally, tetragonal $(CH_3NH_3)PbI_3$ has a centrosymmetric Pb-site symmetry even though the whole structure lacks an inversion center. Etienne *et al.* [26] and Kepenekian and Even [41] noted that Rashba splitting occurs due to breaking a *site* inversion asymmetry. This symmetry argument explains the absence of the Rashba splitting in Fig. 3(d).

Next, we fully relax atomic positions in the tetragonal structure (CCDC deposition No. 1870791) and repeat the calculation of the band structure. The relaxed structure shows a signature of Rashba splitting at the Γ point at the conduction band edge (CBE), although its magnitude is rather weak ($E_R = 5$ meV, Fig. 4), which is comparable to $E_R = 10$ meV found in relativistic quasiparticle calculations [30]. This result implies that the symmetry of the PbI_3 cage is broken after relaxation. The Rashba splitting is more prominent in the conduction band that is mostly composed of Pb-p orbitals (83%)

with a minor contribution from I-p, s (14%). The orbital character at the valence band edge (VBE) has significantly less contribution from lead: I-p (70%) and Pb-s (30%).

To quantify a displacement of the Pb atom from the center of mass of an octahedron formed by iodine atoms [see Fig. 5(a)] we use the following expression:

$$\delta \boldsymbol{r}_{Pb} = \boldsymbol{r}_{Pb} - \frac{1}{6} \sum_{i=1}^{6} \boldsymbol{r}_{I_i}. \tag{8}$$

Here $\boldsymbol{r}_{Pb}$ and $\boldsymbol{r}_{I_i}$ refer to the Cartesian coordinates of the corresponding atomic species. The tetragonal structure with relaxed atomic positions has a displacement of about $\delta r_{Pb} \sim 0.1$ Å. Our results are consistent with the Pb-displacement value of 0.09 Å reported by Liu *et al.* [42] for the tetragonal phase. The displacement in a cubic structure is greater (about 0.25 Å [43]), which results in a larger magnitude of E_R typically found in those structures [44].

To link the magnitude of the Rashba splitting E_R with the displacement of the Pb atom, we performed calculations for a cubic structure ($a = 6.29$ Å) by varying $\delta \boldsymbol{r}_{Pb}$ with I atoms fixed at their perfect positions expressed by the fractional coordinates $(1/2, 0, 0)$ and permutations of that. The most

effective displacement direction for enhanced E_R is along the diagonal of the cube $\langle 111 \rangle$ [Fig. 5(a), CCDC deposition No. 1870792]. The largest Rashba splitting is observed in the k plane that is perpendicular to the displacement vector δr_{Pb}; the splitting vanishes for k paths oriented parallel to the displacement vector.

Results for $E_R(\delta r_{Pb})$ are shown in Fig. 5(b). It is interesting that the same structure with Sn instead of Pb (used as a lead-free alternative to $(CH_3NH_3)PbI_3$ perovskites [45]) shows a comparable E_R in spite of a drastic difference in the SOC constant between Pb and Sn ($\lambda_{SO} = 0.91$ eV vs 0.27 eV [46], respectively). At first this result may look counterintuitive since it is commonly accepted [47] that the Rashba parameter α_R is proportional to λ_{SO}, which leads to the much stronger dependence $E_R \propto \lambda_{SO}^2$. However, the SOC constant λ_{SO} is determined for isolated atoms and serves as an approximation for orbitals that are significantly altered by chemical bonding. Comparable values of E_R for Pb-based and Sn-based structures suggest that the vector product of an effective asymmetric electric field E_0 experienced by electrons and their velocity v averaged over possible trajectories for a given orbital is similar in both cases.

For the splitting energy to reach $k_B T \approx 26$ meV at room temperature, the displacement should be on the order of 0.3 Å [Fig. 5(b)], which is far above the static displacements of Pb atoms in the tetragonal phase of $(CH_3NH_3)PbI_3$. Does the lattice dynamics provide sufficient distortions for the Rashba splitting to exceed 26 meV?

B. Dynamic structures

Now we turn our attention to the dynamic structure of $(CH_3NH_3)PbI_3$. The supercell size selected in our calculations greatly exceeds previous simulations [26,30], which provides a more realistic model for structural fluctuations and allows access to phonon modes that are otherwise not present in smaller cells. Figure 6 shows a time evolution of δr_{Pb}. The dynamic amplitude of δr_{Pb} near room temperature can reach 0.8 Å, and the average displacement stabilizes near 0.37 Å. According to Fig. 5, we would expect a much stronger Rashba splitting in those structures.

Interpretation of band structure calculations of supercells is not straightforward due to a band folding. Here, we used an unfolding technique implemented in the "fold2Bloch" utility [38]. Effective band structures of the $(CH_3NH_3)PbI_3$ supercell, taken at different MD simulation times, are shown in Fig. 7 (structure files can be accessed at CCDC deposition Nos. 1870785–1870790). As anticipated, the initial ($t = 0$) structure features no Rashba splitting [compare Fig. 7(a) and Fig. 3(d)] and serves as a benchmark for comparison with other structures. The Bloch character of primitive wave vectors k (pseudocubic in this case) is well defined for the initial structure, which is indicative of periodicity of the wave function preserved throughout the supercell.

It should be noted that values of the Rashba splitting E_R in Fig. 7 are evaluated with respect to the CBE in the *full* Brillouin zone
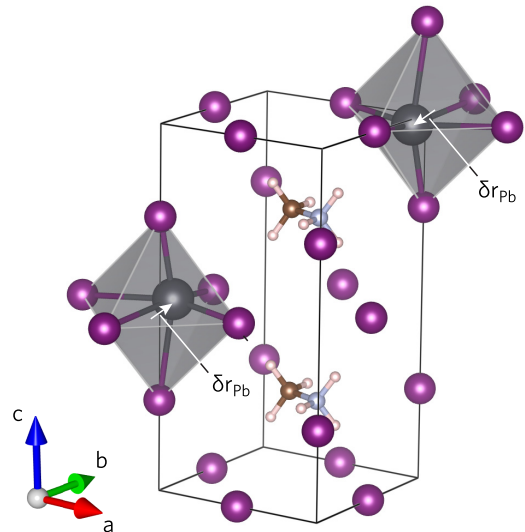
$$E_R = E_{CB}(R) - \min[E_{CB}(k)]. \tag{9}$$

FIG. 8. Perovskite structure with two Pb atoms displaced in opposite directions by the same magnitude.

The energy eigenvalue $\min[E_{CB}(k)]$ may not necessarily lie on the Γ-R-S path selected for the band structures in Fig. 7, which can give the impression of an inconsistency between the band structure and E_R values. At $t = 0.42$ ps, for instance, the CBE unfolds into $k = (1/2, -0.375, 1/2)$ with the Bloch spectral weights of 62%. Since this k point does not belong to the Γ-R-S path, the band structure in Fig. 7(a) does not capture the full extent of the Rashba splitting, whereas E_R does.

In dynamic structures we observe breaking of the Kramers degeneracy with the most pronounced Rashba splitting of $E_R \approx 120$ meV [Fig. 7(b)] observed in the conduction band near the end of the preheating stage ($t = 0.42$ ps). It is a manifestation of the dynamic Rashba splitting present even in centrosymmetric structures [21,28,30]. This time frame corresponds to the maximum average displacement in Fig. 6 and sets an upper limit for dynamic E_R. It is instructive to analyze this result, but it can hardly be physically plausible since the MD displacements of Pb atoms are still coherent at this time. The Rashba splitting gradually decreases as the dynamics of Pb atoms becomes less coherent [Figs. 7(d)–7(f)] even though the average displacement vector $\langle \delta r_{Pb}(t) \rangle$ remains steady at the MD time $t > 2$ ps (Fig. 6). This behavior suggests that not only the displacement magnitude but also a mutual orientation of displacement vectors play a role in determining E_R.

To verify this hypothesis, we created a supercell where Pb atoms in two PbI_6 octahedra had equal displacements by magnitude but opposite in direction ($\delta r_{Pb1} = -\delta r_{Pb2}$) as shown in Fig. 8 (CCDC deposition No. 1870793). In spite of sizable displacements ($\delta r_{Pb} = 0.5$ Å), the Rashba splitting completely vanishes in this structure. To rationalize this result, we recall that the effective asymmetric electric field E_0 that causes Rashba splitting is aligned with the displacement δr_{Pb}. When atoms are displaced in opposite directions, the electric field on each atomic site opposes the other leading to cancellation of the net effective electric field. This reasoning explains why dynamic structures have a small E_R despite a relatively large average displacement.
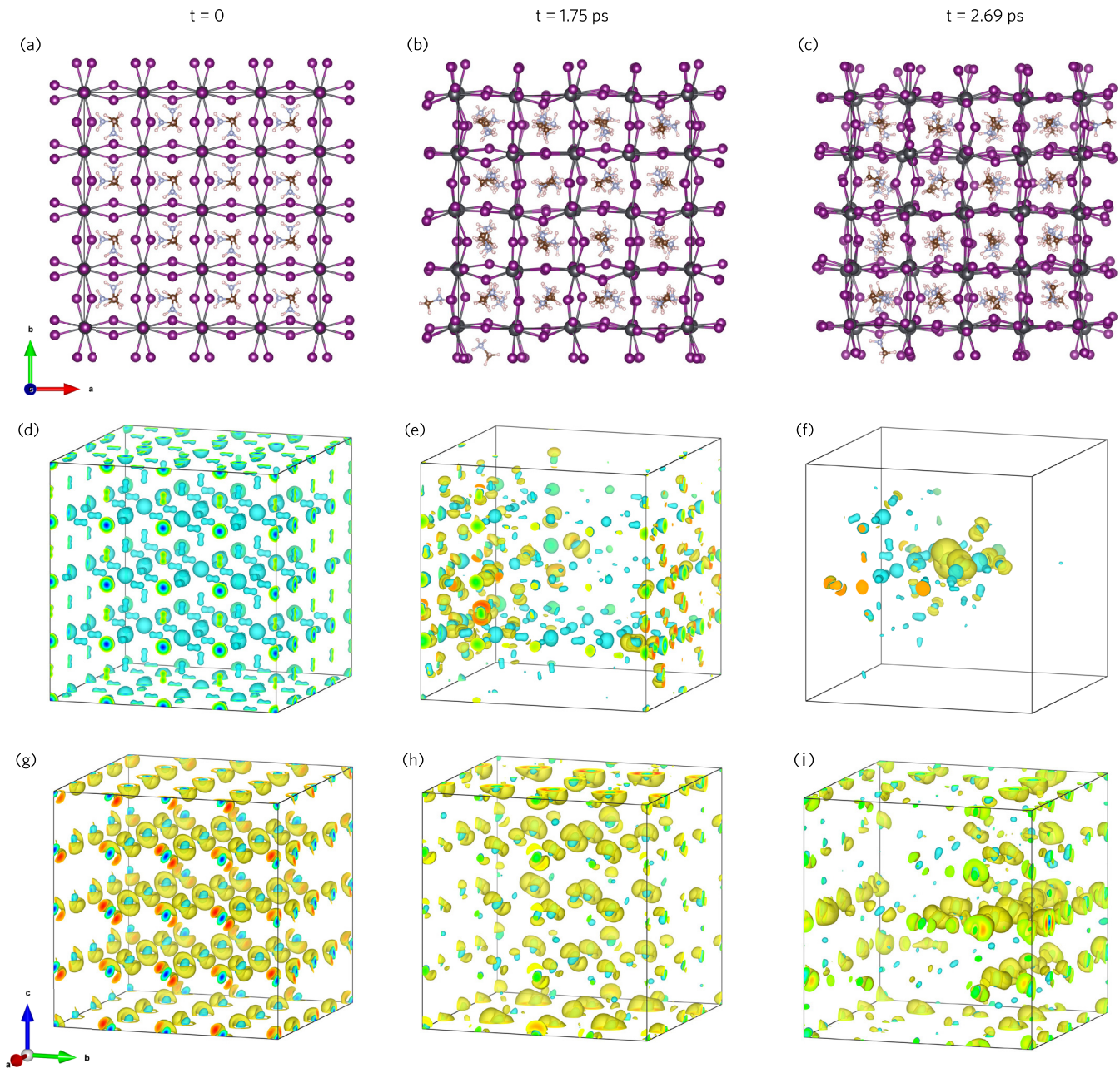
FIG. 9. (a)–(c) $4 \times 4 \times 4$ tetragonal $(CH_3NH_3)PbI_3$ supercell structure at different MD time steps and the corresponding spatial distribution of DFT orbitals $\psi_i(\boldsymbol{r})$ for (d)–(f) VBE and (g)–(i) CBE states. Isosurfaces correspond to the values of $\psi = \pm 5 \times 10^{-4}$.

Next, we discuss the valence band. In Fig. 7, the valence band becomes too disordered to make any conclusions about Rashba splitting there. This result suggests that k is not a good quantum number for holes in the dynamic structure of $(CH_3NH_3)PbI_3$. The loss of Bloch character at the VBE undermines the argument about an indirect band gap [Fig. 1(b)], which implies that Δk is well resolved. Instead, the prolonged carrier lifetime can originate from a weak overlap in real and reciprocal space between extended electron states and localized hole states.

For solar cells it is important to have a material with good bipolar transport properties. It is known that mobility decreases with T due to electron-phonon scattering, which is also true for perovskites [48]. The question is whether the charge transport coefficients of electrons and holes are equally susceptible to thermal structural fluctuations. To address this question, we plot the wave function of electronic eigenstates at the VBE and CBE in Fig. 9. The structural fluctuations impact the spatial coherency of wave functions at the band edges. Electronic states at the VBE undergo the most significant changes which eventually leads to their spatial localization [Fig. 9(f)]. Electronic states at the CBE seem to be more robust against thermal structural fluctuations, which is also consistent with their better ability to retain the Bloch character (Fig. 7).

To further explore possible localization of electronic eigenstates, we present IPR spectra in Fig. 10 for structures at different MD time snapshots. IPR represents the inverse number
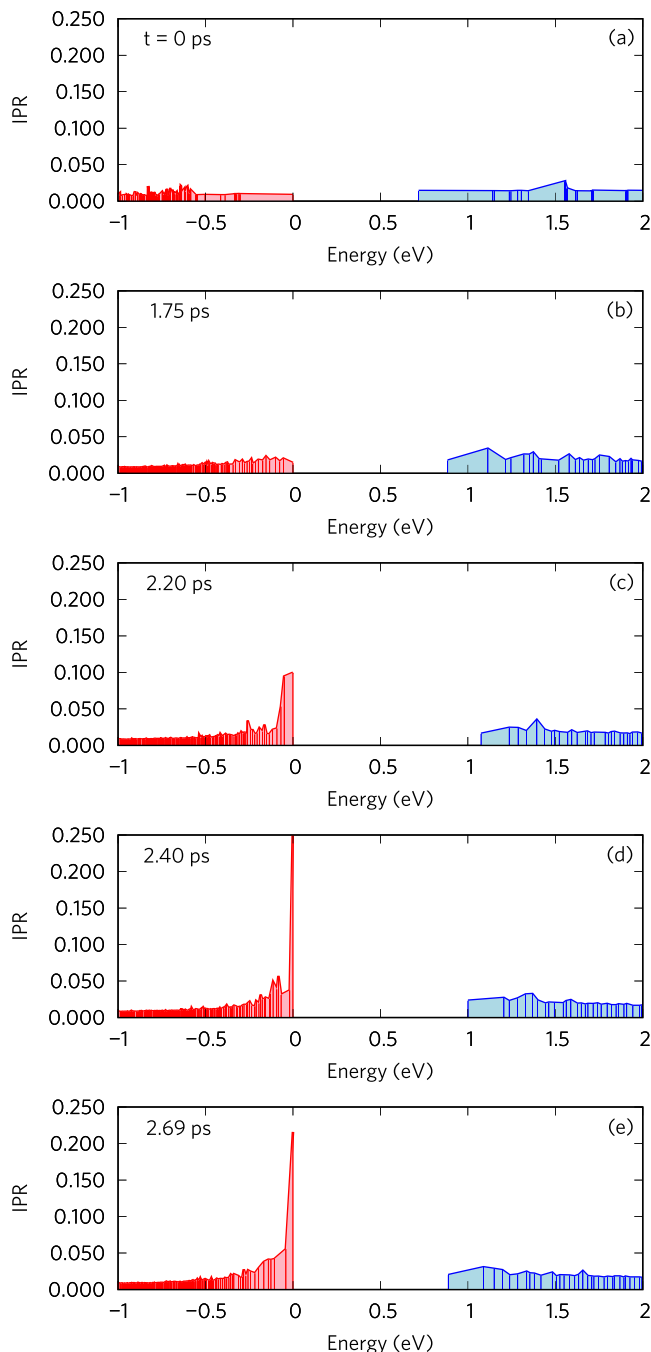
FIG. 10. Spectrally resolved inverse participation ratio for states in vicinity of the band gap of $4 \times 4 \times 4$ tetragonal $(CH_3NH_3)PbI_3$ supercell taken at different MD time snapshots: (a) $t = 0$, (b) 1.75 ps, (c) 2.2 ps, (d) 2.4 ps, and (e) 2.69 ps. A spatial localization of the DFT orbitals takes place at the valence band edge due to dynamic atomic displacements. The structural fluctuations open the band gap, which continues to change dynamically.

of atoms that contribute to an eigenstate. Localized states exhibit higher IPR values. The initial structure [Fig. 10(a)] sets a baseline for the IPR spectrum in the case of a localization-free structure. The IPR spectrum shows a clear distinction between structures at 1.75 and 2.69 ps. A spike in the IPR spectrum at the VBE [Fig. 10(e)] confirms localization of these states.

Additional spectra obtained at MD times of 2.2 and 2.4 ps [Figs. 10(c) and 10(d)] confirm that the localization in the VBE is a persistent feature, not a random occurrence. Thus, we would expect the mobility of holes in $(CH_3NH_3)PbI_3$ to be much more sensitive to thermal structural fluctuations (phonon scattering) than the mobility of electrons. This result is consistent with a steeper increase of the effective mass of holes with temperature predicted earlier [49].

By observing changes in the band gap in Fig. 10, we can conclude that the dynamic structural disorder opens up the band gap substantially as also noticed by Saidi *et al.* [50] and McKechnie *et al.* [30]. After opening, the band gap continues to change dynamically with fluctuations of $\sim$0.3 eV, which is consistent with the literature [28,50]. It is interesting to note that the band gap renormalization of such a large magnitude due to the structural dynamic is inherent to wide band gap materials only. Furthermore, the renormalization typically leads to a *decrease* of the band gap [51] contrary to what is observed in perovskites where the gap widens.

Finally, we would like to comment on a spin texture at the band edges of perovskites. The long carrier lifetime is sometimes also attributed to spin-forbidden optical transitions rooted in the Rashba splitting [12]. Figure 11 presents the band structure of cubic $(CH_3NH_3)PbI_3$ [$\delta_{Pb} = 0.54$ Å, Fig. 5(a)] with three spin projections $\langle S_x \rangle$, $\langle S_y \rangle$, and $\langle S_z \rangle$. The Rashba valleys show a spin splitting with the symmetry $E(\mathbf{k}, \mathbf{S}) = E(-\mathbf{k}, -\mathbf{S})$ leading to a spin helicity. Optical transitions between CBE and VBE are hindered, provided the initial and final states have an opposite spin helicity. However, this is not the case in Fig. 11 where CBE and VBE have *similar* spin projections. Using spin projections it is possible to determine spinor components (α and β, see Sec. II) and the spin overlap at the band edges. Results presented in Table I indicate an almost perfect spin overlap of 99% between the two states representing CBE and the corresponding top of the valence band shown by the arrow in Fig. 11(c). The spin overlap remains high (greater than 90%) in the tetragonal phase of $(CH_3NH_3)PbI_3$ (Table I). Examination of spin states in two dynamic structures ($t = 0.42$ and 2.69 ps, Table I) reveals no changes in this trend. Thus, we reach the conclusion that the spin helicity poses no barriers for recombination of optical excitations in $(CH_3NH_3)PbI_3$ contrary to Ref. [12].

IV. CONCLUSIONS

The extended carrier lifetime in hybrid halide perovskites was attributed to a quasi-indirect band gap that arises due to Rashba splitting in both conduction and valence band edges. In this paper we calculated the effective relativistic band structure of $(CH_3NH_3)PbI_3$ with the focus on the dispersion of electronic states near the band edges of $(CH_3NH_3)PbI_3$ affected by thermal structural fluctuations. The disorder is explicitly modeled via *ab initio* molecular dynamics simulation performed for a large supercell. A semiempirical scaling of the lattice parameters was used to achieve a finite-temperature structure of $(CH_3NH_3)PbI_3$.

Our preliminary studies involving static structures indicated that a tetragonal $(CH_3NH_3)PbI_3$ with the PbI_3 cage symmetry fixed to that obtained from x-ray diffraction studies shows no Rashba splitting even though the whole structure
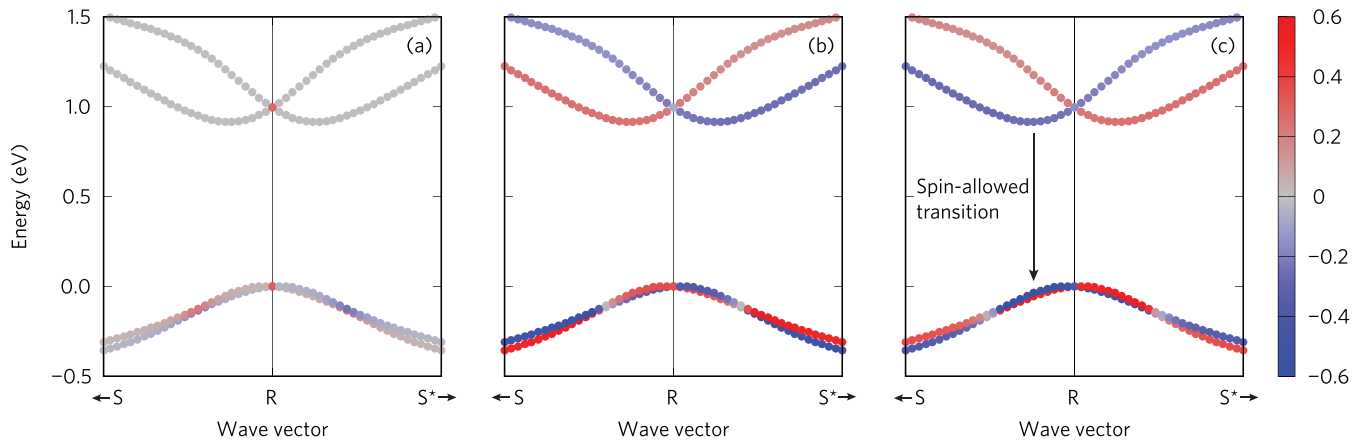
FIG. 11. Spin texture (a) $\langle S_x \rangle$, (b) $\langle S_y \rangle$, and (c) $\langle S_z \rangle$ in a symmetrized unit cell of cubic $(CH_3NH_3)PbI_3$ with Pb atom displaced by 0.54 Å along the [111] direction from the center of an octahedron formed by iodine atoms [Fig. 5(a), CCDC deposition No. 1870792].

lacks the inversion center. This result is attributed to a centrosymmetric Pb-site symmetry. The fully relaxed tetragonal structure showed a weak Rashba splitting ($E_R = 5$ meV), which occurs due to breaking a Pb-atom site inversion symmetry. For the splitting energy to reach $k_BT \approx 26$ meV at room temperature, the displacement should be on the order of 0.3 Å, which is far above the static displacements of Pb atoms in the tetragonal phase of $(CH_3NH_3)PbI_3$. Remarkably, lead-free perovskite structures (with Pb substituted by Sn while keeping the geometry the same) show a comparable E_R despite a drastic difference in the spin-orbit coupling constants.

The dynamic average displacement of Pb atoms amounts to 0.37 Å at room temperature with the amplitude reaching 0.8 Å. The band structure of supercells taken at different time snapshots during molecular dynamics simulation were unfolded to a primitive (pseudocubic) Brillouin zone. The most pronounced Rashba splitting of $E_R \approx 120$ meV is observed when the dynamics of Pb atoms is still coherent. The dynamic Rashba splitting diminishes down to 4 meV as the molecular

dynamics progresses to longer times (beyond 2 ps), which is assigned to randomization of Pb-displacement vectors and associated cancellation of the net effective magnetic field acting on electrons at the conduction band edge. At the same time, the valence band becomes disordered and loses the Bloch character that undermines the argument about an indirect band gap present in the dynamic structure of $(CH_3NH_3)PbI_3$ at room temperature. Analysis of the spatial distribution of DFT orbitals at the valence band edge reveals their spatial localization in the dynamic structures as also confirmed by the inverse participation ratio spectra. Electronic states at the conduction band edge are more robust against thermal structural fluctuations, which is also consistent with their better ability to retain the Bloch character. Thus, the mobility of holes should be much more susceptible to phonon scattering than the mobility of electrons. The finite-temperature structural dynamics opens the band gap that continues to fluctuate with the amplitude of ~ 0.3 eV at the sub-picosecond time scale. Analysis of spin projections

TABLE I. Spin texture and spin overlap between the conduction band edge and the valence band in different structures of $(CH_3NH_3)PbI_3$.

Parameter	cubic [$\delta_{Pb} = 0.54$ Å, Fig. 5(a)]	tetragonal	MD ($t = 0.42$ ps)	MD ($t = 2.69$ ps)
Conduction band edge				
Wave vector $\boldsymbol{k}$	[0.44, 1/2, 1/2]	[0.02, 0, 0]	[0, 1/2, 0]	[0, 0, 0.111]
Unfolded $\boldsymbol{k}$ (Bloch character)			[1/2, −0.375, 1/2] (62%)	[1/2, 1/2, 0.472] (56%)
$\langle S_x \rangle$	0.008	−0.026	−0.086	0.154
$\langle S_y \rangle$	0.238	0.192	−0.001	−0.028
$\langle S_z \rangle$	−0.245	−0.089	0.083	−0.008
Spin up α ($|\alpha|^2$)	−0.376 + 0i (14%)	−0.539 + 0i (29%)	−0.920 + 0i (85%)	0.690 + 0i (48%)
Spin down β ($|\beta|^2$)	−0.030 − 0.926i (86%)	0.098 − 0.836i (71%)	0.392 + 0.006i (15%)	0.712 − 0.130i (52%)
Valence band				
$\langle S_x \rangle$	0.063	−0.021	−0.033	0.228
$\langle S_y \rangle$	0.322	0.367	−0.035	−0.043
$\langle S_z \rangle$	−0.524	−0.452	0.135	−0.187
Spin up α ($|\alpha|^2$)	0.276 + 0i (8%)	0.335 + 0i (11%)	0.985 + 0i (97%)	0.432 + 0i (19%)
Spin down β ($|\beta|^2$)	0.185 + 0.943i (92%)	−0.054 + 0.941i (89%)	−0.118 − 0.123i (3%)	0.887 − 0.167i (81%)
Spin overlap $|\langle \psi_v | \psi_c \rangle|^2$ (%)	99	95	91	90

and the spin overlap at the band edges rules out spin helicity as a possible mechanism for a long lifetime of optical excitations in perovskite structures.

ACKNOWLEDGMENTS

[1] A. Kojima, K. Teshima, Y. Shirai, and T. Miyasaka, J. Am. Chem. Soc. **131**, 6050 (2009).

[2] M. M. Lee, J. Teuscher, T. Miyasaka, T. N. Murakami, and H. J. Snaith, Science **338**, 643 (2012).

[3] M. Grätzel, Nat. Mater. **13**, 838 (2014).

[4] K. A. Bush, A. F. Palmstrom, Z. J. Yu, M. Boccard, R. Cheacharoen, J. P. Mailoa, D. P. McMeekin, R. L. Z. Hoye, C. D. Bailie, T. Leijtens *et al.*, Nat. Energy **2**, 17009 (2017).

[5] T. Singh and T. Miyasaka, Adv. Energy Mater. **8**, 1700677 (2018).

[6] Y. Yamada, T. Yamada, L. Q. Phuong, N. Maruyama, H. Nishimura, A. Wakamiya, Y. Murata, and Y. Kanemitsu, J. Am. Chem. Soc. **137**, 10456 (2015).

[7] D. Bi, W. Tress, M. I. Dar, P. Gao, J. Luo, C. Renevier, K. Schenk, A. Abate, F. Giordano, J.-P. Correa Baena *et al.*, Sci. Adv. **2**, e1501170 (2016).

[8] Y. Bi, E. M. Hutter, Y. Fang, Q. Dong, J. Huang, and T. J. Savenije, J. Phys. Chem. Lett. **7**, 923 (2016).

[9] T. Handa, D. M. Tex, A. Shimazaki, A. Wakamiya, and Y. Kanemitsu, J. Phys. Chem. Lett. **8**, 954 (2017).

[10] X. Ziang, L. Shifeng, Q. Laixiang, P. Shuping, W. Wei, Y. Yu, Y. Li, C. Zhijian, W. Shufeng, D. Honglin *et al.*, Opt. Mater. Express **5**, 29 (2015).

[11] J. Even, L. Pedesseau, J. M. Jancu, and C. Katan, Phys. Status Solidi Rapid Res. Lett. **8**, 31 (2014).

[12] F. Zheng, L. Z. Tan, S. Liu, and A. M. Rappe, Nano Lett. **15**, 7794 (2015).

[13] M. Kepenekian, R. Robles, C. Katan, D. Sapori, L. Pedesseau, and J. Even, ACS Nano **9**, 11557 (2015).

[14] G. Dresselhaus, Phys. Rev. **100**, 580 (1955).

[15] E. I. Rashba and V. I. Sheka, Fiz. Tverd. Tela: Collected Papers **2**, 162 (1959).

[16] G. Bihlmayer, O. Rader, and R. Winkler, New J. Phys. **17**, 050202 (2015).

[17] C. Katan, L. Pedesseau, M. Kepenekian, A. Rolland, and J. Even, J. Mater. Chem. A **3**, 9232 (2015).

[18] P. Azarhoosh, S. McKechnie, J. M. Frost, A. Walsh, and M. van Schilfgaarde, APL Mater. **4**, 091501 (2016).

[19] T. Wang, B. Daiber, J. M. Frost, S. A. Mann, E. C. Garnett, A. Walsh, and B. Ehrler, Energy Environ. Sci. **10**, 509 (2017).

[20] D. Niesner, M. Wilhelm, I. Levchuk, A. Osvet, S. Shrestha, M. Batentschuk, C. Brabec, and T. Fauster, Phys. Rev. Lett. **117**, 126401 (2016).

[21] D. Niesner, M. Hauck, S. Shrestha, I. Levchuk, G. J. Matt, A. Osvet, M. Batentschuk, C. Brabec, H. B. Weber, and T. Fauster, Proc. Natl. Acad. Sci. USA **115**, 9509 (2018).

[22] E. Menéndez-Proupin, P. Palacios, P. Wahnón, and J. C. Conesa, Phys. Rev. B **90**, 045207 (2014).

[23] F. Brivio, K. T. Butler, A. Walsh, and M. van Schilfgaarde, Phys. Rev. B **89**, 155204 (2014).

[24] P. S. Whitfield, N. Herron, W. E. Guise, K. Page, Y. Q. Cheng, I. Milas, and M. K. Crawford, Sci. Rep. **6**, 35685 (2016).

[25] G. M. Bernard, R. E. Wasylishen, C. I. Ratcliffe, V. Terskikh, Q. Wu, J. M. Buriak, and T. Hauger, J. Phys. Chem. A **122**, 1560 (2018).

[26] T. Etienne, E. Mosconi, and F. De Angelis, J. Phys. Chem. Lett. **7**, 1638 (2016).

[27] B. Monserrat and D. Vanderbilt, Phys. Rev. Mater. **1**, 054201 (2017).

[28] B. Monserrat and D. Vanderbilt, arXiv:1711.06274.

[29] T. Etienne, E. Mosconi, and F. De Angelis, J. Phys. Chem. C **122**, 124 (2018).

[30] S. McKechnie, J. M. Frost, D. Pashov, P. Azarhoosh, A. Walsh, and M. van Schilfgaarde, Phys. Rev. B **98**, 085108 (2018).

[31] G. Kresse and J. Furthmüller, Phys. Rev. B **54**, 11169 (1996).

[32] G. Kresse and J. Furthmüller, Comput. Mater. Sci. **6**, 15 (1996).

[33] W. Kohn and L. J. Sham, Phys. Rev. **140**, A1133 (1965).

[34] J. P. Perdew, K. Burke, and M. Ernzerhof, Phys. Rev. Lett. **77**, 3865 (1996).

[35] S. Grimme, J. Antony, S. Ehrlich, and H. Krieg, J. Chem. Phys. **132**, 154104 (2010).

[36] C. C. Stoumpos, C. D. Malliakas, and M. G. Kanatzidis, Inorg. Chem. **52**, 9019 (2013).

[37] H. J. Monkhorst and J. D. Pack, Phys. Rev. B **13**, 5188 (1976).

[38] O. Rubel, A. Bokhanchuk, S. J. Ahmed, and E. Assmann, Phys. Rev. B **90**, 115202 (2014).

[39] N. C. Murphy, R. Wortis, and W. A. Atkinson, Phys. Rev. B **83**, 184206 (2011).

[40] C. Pashartis and O. Rubel, Phys. Rev. Appl. **7**, 064011 (2017).

[41] M. Kepenekian and J. Even, J. Phys. Chem. Lett. **8**, 3362 (2017).

[42] S. Liu, F. Zheng, I. Grinberg, and A. M. Rappe, J. Phys. Chem. Lett. **7**, 1460 (2016).

[43] W.-L. Yan, G.-H. Lu, and F. Liu, J. Phys. Chem. C **120**, 17972 (2016).

[44] S. Hu, H. Gao, Y. Qi, Y. Tao, Y. Li, J. R. Reimers, M. Bokdam, C. Franchini, D. Di Sante, A. Stroppa *et al.*, J. Phys. Chem. C **121**, 23045 (2017).

[45] P. V. Kamat, J. Bisquert, and J. Buriak, ACS Energy Lett. **2**, 904 (2017).

[46] K. Wittel and R. Manne, Theor. Chim. Acta **33**, 347 (1974).

[47] S. Picozzi, Front. Phys. **2**, 1 (2014).

[48] R. L. Milot, G. E. Eperon, H. J. Snaith, M. B. Johnston, and L. M. Herz, Adv. Funct. Mater. **25**, 6218 (2015).

[49] Y.-B. Lu, H. Yang, W.-Y. Cong, P. Zhang, and H. Guo, Appl. Phys. Lett. **111**, 253902 (2017).

[50] W. A. Saidi, S. Poncé, and B. Monserrat, J. Phys. Chem. Lett. **7**, 5247 (2016).

[51] M. Cardona and M. L. W. Thewalt, Rev. Mod. Phys. **77**, 1173 (2005).